Journal of Materials, Processing and Design (2024)
Clausius Scientific Press, Canada

DOI: 10.23977/jmpd.2024.080213
ISSN 2516-0923 Vol. 8 Num. 2

Low temperature colloidal synthesis of carbon coated Prussian blue cathode for high-rate and long-life sodium-ion batteries

Xianliu Lu, Ning Li, Jinwang Feng, Bingxin Lei*

School of Materials and Environment, Guangxi Key Laboratory of Advanced Structural Materials and Carbon Neutralization, Guangxi Colleges and Universities Key Laboratory of Eco-friendly Materials and Eco-Restoration, Guangxi Minzu University, Nanning, 530105, China
**Corresponding author: leibx@gxmzu.edu.cn*

Keywords: Prussian blue, Carbon collosol, High rate, Long lifespan, Sodium-ion batteries

Abstract: Prussian blue (PB) cathodes are plagued by subpar rate capability and inadequate cycling performance, which stem from their low electronic conductivity and side reactions with the electrolyte. Carbon coating represents an effective solution to this issue. Nevertheless, it cannot fully encapsulate cathode materials. In this study, we synthesize carbon sol using starch as a precursor and successfully encapsulate the carbon on the surface of PB to form PB@C through the liquid phase method at low temperature. The carbon coating can effectively prevent PB from being corroded by the electrolyte during the cycling process and accelerate the transfer of electrons. The PB@C cathode demonstrates a significant capacity of 169 mAh g^{-1} at a low rate of 0.1C, approaching its theoretical specific capacity, and it is capable of retaining a capacity of 85 mAh g^{-1} even at a high rate of 30C. The material demonstrates impressive high-rate cycling performance, maintaining a capacity of 70 mAh g^{-1} and achieving a capacity retention rate of 76.7% after undergoing 1000 cycles at a rate of 20C. This outstanding rate capability and cycling stability are ascribed to the carbon coating layer, which can boost the electron transfer among materials, enhances the diffusion coefficient for sodium ions, and improves structural integrity. These outcomes imply that the PB@C material holds exceptional promise as a cathode for sodium–ion batterie.

1. Introduction

For three decades, advancements in lithium-ion batteries (LIBs) have successfully tackled energy scarcity issues and emerged as a key solution for energy storage, becoming an integral part of our everyday lives[1, 2]. Nevertheless, the high costs associated with lithium batteries and the uneven availability of lithium resources make it essential to investigate alternative battery technologies[3, 4]. Compared with LIBs, sodium-ion batteries (SIBs) exhibit superior safety, abundant availability, and lower costs, thereby demonstrating remarkable suitability as large-scale energy storage technology [5, 6]. Through relentless research endeavors, scientists have pinpointed several dependable cathode materials, including Prussian blue (PB), layered oxides, and poly-anion

compounds [7, 8]. PB emerges as a highly noteworthy material, garnering heightened interest owing to its exceptional theoretical specific capacity, surpassing that of conventional transition metal oxides and polyanion compounds. Furthermore, PB stands out for its inherent rigidity within an open framework, cost-effectiveness, and non-toxic properties [9, 10]. However, for PB cathodes, to enhance the rate performance and cycling performance of PB, it is necessary to tackle the challenges related to tackle the challenges related to low electronic conductivity and electrolyte erosion during cycling.

Numerous synthesis strategies have been developed to mitigate the adverse effects on the electrochemical performance of PB materials, including surface modification, surface coating, and the formation of composites with conductive materials, etc [11, 12]. For these strategies, the electrical contact can be effectively enhanced by suppressing mechanical fracture of the electrode [13]. Despite the fact that the entire or partial surface of PB remains exposed, this leads to PB being perpetually impacted by the side reactions of the electrolyte throughout the cycling process. Consequently, its sodium storage performance is also continually compromised. This urges the necessity of employing conductive composite materials to coat PB particles, thereby preventing PB particles from being constantly encroached upon by the electrolyte side reactions throughout the cycling process [14, 15]. Coating the surface of PB with carbon represents an effective method for modification. However, the preparation of PB@C cathode is not a straightforward process, as these carbon materials have a tendency to agglomerate [16], resulting in non-uniform dispersion on surface of PB particles. The widely reported method of carbon coating has been shown to improve the electrochemical performance of layered oxide and polyanion electrode materials [17, 18]. However, akin to carbon coated layered oxides and polyanion cathodes, the practical preparation of carbon-coated PB is impeded by its propensity to decompose at high temperature. It is desirable to achieve high-rate and long-life SIBs cathodes by applying carbon coating layer on the surface of PB at low temperature through a solution-based method.

Herein, we prepared a low-cost carbon-coated PB composites (PB@C) using a straightforward liquid phase method at low temperature. $Na_4Fe(CN)_6$ was utilized as the sole precursor, which underwent self-decomposition to yield PB under acidic conditions. Furthermore, a carbon sol was integrated into the synthesis process of PB, wherein the Fe^{2+}/Fe^{3+} resulting from the self-decomposition of $[Fe(CN)_6]^{4-}$, and a carbon coating layer is produced, resulting in the formation of PB@C. Introducing a carbon coating layer can enhance the electrical conductivity PB, facilitating superior ion transport during charging and discharging processes and increasing the capacity contribution from the surface capacitance process. Consequently, the carbon coating layer derived from carbon sol leaded to exceptional performance at high current densities.

2. Experimental procedures

2.1 Chemicals and Reagents

The starch is purchased from Aladdin Reagent Co. Sodium ferrocyanide ($Na_4Fe(CN)_6$, 99%) and Hydrochloric acid (37%) were purchased from Adamas.

2.2 Synthesis of carbon sol

Synthesis of carbon sols: 0.3 g of starch were dissolved in 25 mL of deionized water and stirred at 60 ℃ for 10 min. Subsequently, the mixture was promptly placed into a 50 mL high-pressure reaction kettle and heated in an oven at 190 ℃ for 2 h to yield a brown solution.

2.3 Synthesis of PB and PB@C

Synthesis of PB and PB@C: Prepare PB in the same way as previously reported [19]. Dissolve 2 mmol of sodium ferrocyanide in the previously prepared carbon sol solution. Then, add 0.5 mL of hydrochloric acid to the resulting mixture. Stir the combination at 60 ℃ for 4 h. Subsequently, after a series of centrifugation, cleaning, and drying processes, the PB@C sample was collected. For the PB, deionized water was used instead of carbon sol.

2.4 Characterizations

The X-ray diffraction data were acquired at 25°C with a scanning step of 0.02° and the 2θ range was established from 10 ° to 70 °. Microstructures and morphologies of the samples were analyzed using a SEM (SUPRA 55 Sapphire) and a TEM (FEI, tecnai F20). The Raman spectra of materials were determined by means of the LabRam HR Evolution. The infrared spectrum of the material was determined via a Fourier Transform Infrared (FT-IR) spectrometer produced by Shimadzu, Japan.

2.5 Electrochemical measurements

The electrode material (70%, weight %), ketjen black (20%, weight %), was meticulously blended with PVDF (10%, weight%). Following this, NMP was introduced and the mixture was thoroughly stirred to ensure the formation of a homogeneous slurry. This slurry was then uniformly coated onto aluminum foil. Subsequently, the coated foil underwent vacuum drying at a temperature of 80 ℃throughout the night to yield the electrode sheet. The NaClO4 (1 M) electrolyte (EC: PC = 1: 1 vol%), supplemented with 5% FEC, was employed. The LAND system was employed to conduct cycling and rate performance tests within the voltage range from 2.0 to 4.0 V. The cyclic voltammograms (CV) at various scanning rates were acquired using the electrochemical workstation (CHI760E, Chenhua, Shanghai) within a voltage range of 2.0-4.0 V.

3. Results and discussion

3.1 Structure and morphology

Figure 1a presents the comparison of XRD patterns of PB and PB@C. For both PB and PB@C samples, the characteristic peaks were accurately matched to the standard card of ferric ferrocyanide JCPDS NO.73-0687. This finding conclusively suggests that both samples possess a face-centered cubic crystal lattice configuration, belonging to the space group $Fm\bar{3}m$. The sharp and strong peaks clearly indicate that both samples contain well-crystallized PB, emphasizing their high degree of crystallinity. It is noteworthy that, for the PB@C samples, the absence of any distinct peaks corresponding to carbon is mainly due to the highly crystalline nature of the PB sample. The outcomes highlights that the incorporation of carbon sol has no influence on the crystal structure of PB, thus preserving its integrity and inherent properties.

The existence of carbon within the PB@C material is verified through Raman spectroscopy, with the resulting spectra displayed in Figure 1b. In Figure1b, the two prominent peaks of carbon centered at 1595 and 1345 cm^{-1} correspond to the G-band and D-band [20], respectively. The two salient peaks are indicative of disordered sp2 carbon. The intensity of G-band surpasses that of the D-band, signifying that carbon contains a lower number of lattice defects, which makes PB@C perform better than PB. Consequently, this outcome indicates the existence of carbon within PB@C. The interaction between PB and carbon can effectively boost its electrical conductivity and facilitate electron transfer among PB samples, leading to outstanding performances in both cycling

and rate capabilities.

The chemical compositions of PB and PB@C were ascertained by means of FT-IR. Figure 1c depicts the infrared spectrograms of PB@C and PB. The strong absorption peak at 2080 cm^{-1} is attributed to the characteristic vibration of the –C≡N–group. The absorption band at around 495 cm^{-1} indicates the existence of Fe-CN-Fe stretching vibrations. The peak observed at 600 cm^{-1} belongs with the stretching vibration of Fe-CN. Upon comparing the FT-IR spectra of PB and PB@C, a minor and indistinct peak at 1300 cm^{-1} is discovered in PB@C, which originates from the stretching vibration of C-C single bonds. This result confirms the presence of carbon within PB@C.

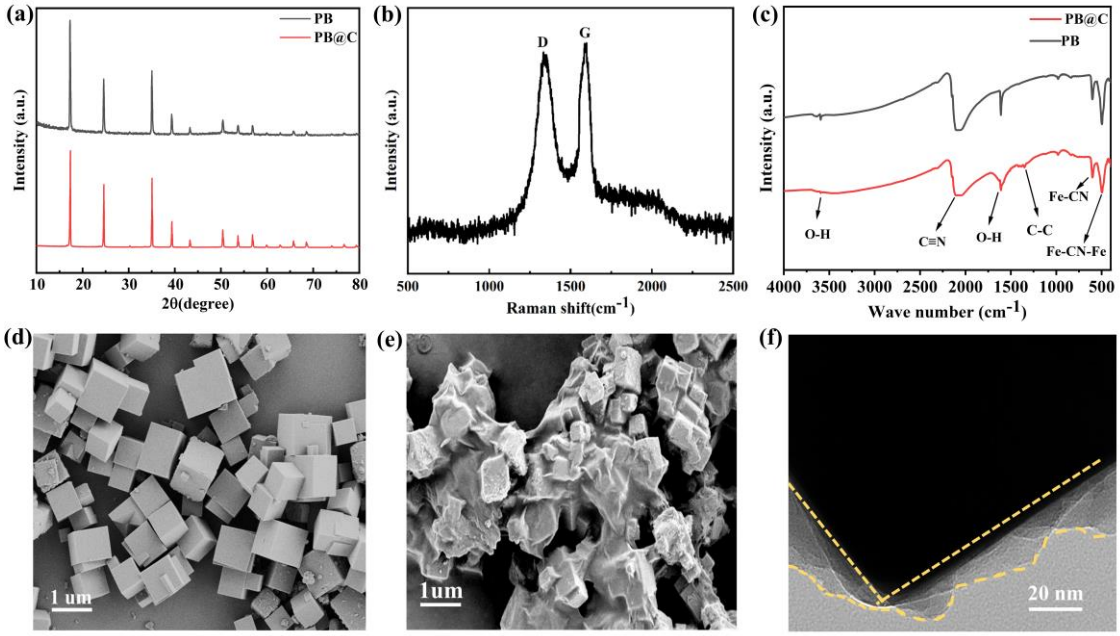

Figure 1: (a) XRD patterns of PB@C and PB; (b) Raman spectroscopy analysis of PB@C; (c) FT-IR spectra of PB and PB@C; SEM images of PB (d) and PB@C (e); (f) TEM image of PB@C.

The morphology of PB and PB@C cathode materials was characterized using SEM and TEM. The SEM image (see Figure 1d) reveals that PB displays a unique microcube structure featuring well-defined edges and its dimensions vary between 400 nm and 1 μm. When PB is treated with carbon sol, it preserves its microcube morphology; however, the surface becomes enveloped in a material resembling yarn. This phenomenon indicates the presence of a carbon coating layer, forming PB@C structure (see Figure 1e). Upon examining the TEM image (see Figure 1f), it becomes evident that the PB@C cube is enveloped by a consistent layer of carbon across its regular cubic surfaces. This carbon coating layer significantly diminishes the material's susceptibility to electrolytic erosion. The synthetic colloidal carbon-coated PB, featuring a uniformly surface with a seamlessly continuous wrapping layer, distinguishes itself from conventional mixed preparations. This innovative methodology is especially well-suited for utilization in SIBs.

3.2 Half-cell performance

Both PB and PB@C composites are employed as cathodes, and sodium foil serves as the anode. These components are assembled into coin cells and subjected to electrochemical tests. The CV curves of PB@C were recorded across a voltage interval of 2.0 to 4.0 V. The CV curves of PB@C acquired at diverse scanning rates are shown in Figure 2a. As depicted in Figure 2a, when the sweep rate is 0.1 mV s^{-1}, the two pairs of cathodic/anodic peaks emerging at 2.78/3.08 V and 3.77/3.80 V

signify the existence of FeHS (N) and FeLS (C) pairs, indicating that the insertion/extraction of sodium ions proceeds in two steps [21]. The FeHS (N) pair, comprising Fe^{2+} coordinated with nitrogen, is in correspondence with the oxidation of high-spin Fe^{2+} and the reduction of Fe^{3+}. Conversely, the FeLS (C) couple, comprising Fe^{2+} bound to carbon, is associated with the oxidation of low-spin Fe^{2+} and the reduction of Fe^{3+}. The oxidation peak shifts towards a higher voltage with the increase of the scanning rate. In contrast, due to polarization, the reduction peak shifts towards a lower voltage.

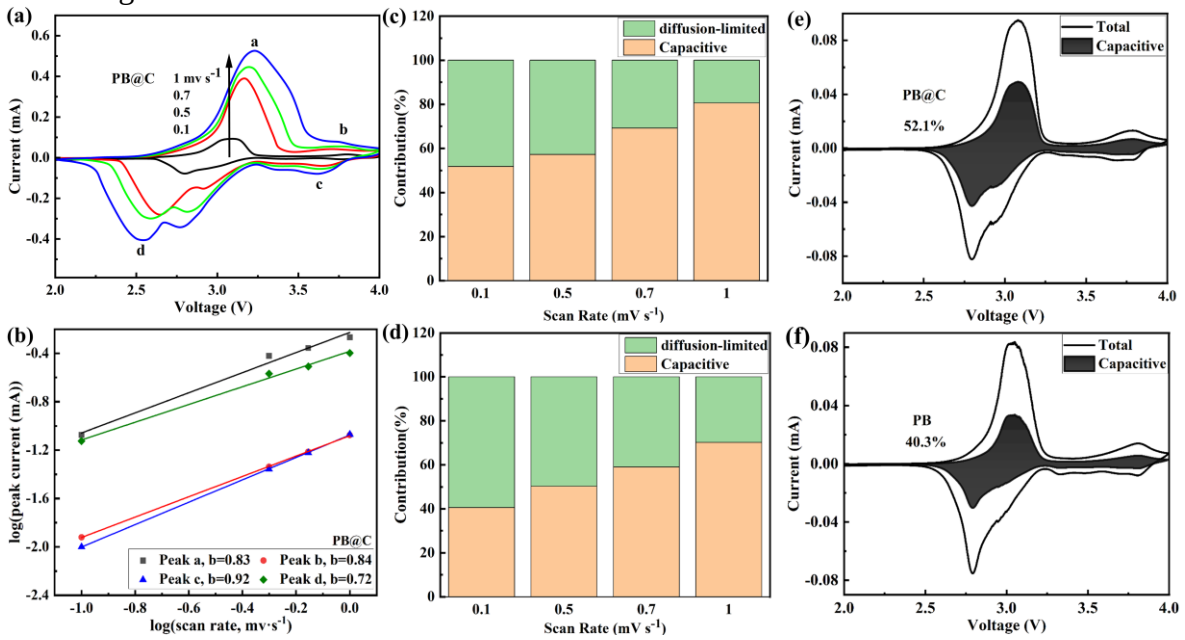

Figure 2: (a) PB@C CV curves under different scanning rates; (b) The log(i) and log(v) fittings of PB@C correspond to the b value of each peak; The capacitance contribution ratio of PB@C (c) and PB (d); The percentage of surface capacitance of PB@C (e)and PB (f) at 0.1 mV s^{-1}.

To explore the charging and discharging mechanisms PB@C, a kinetic analysis of the materials was conducted. In Figure 2a, the two anodic peaks are labeled as a and b, while the two cathodic peaks are labeled as c and d. The connection between current (i) and scanning rate (v) can be fitted by Equation (1)[22].

$$i_p = av^b \tag{1}$$

Where 'a' and 'b' represent variable with adjustable constant, and 'ip' denotes the peak current value of the redox peaks. When the value of b approaches 0.5, the predominant process in the battery's charge-discharge cycle is diffusion insertion. Conversely, when the b value is approximate to 1, the charging and discharging procedures are preponderantly regulated by the surface capacitance mechanism. As shown in Figure 2b, the b-values of peaks (a, b, c, and d) are obtained by fitting Equation (1). Furthermore, the distribution of b-values indicates that both diffusive insertion and surface capacitive processes govern the charging and discharging mechanisms. To contrast the roles of the surface capacitance process and the diffusion insertion process during charging and discharging, we have quantified their respective contributions through the application of Equation (2) [23, 24].

$$i = k_1 v + k_2 v^{0.5} \tag{2}$$

In this Equation (2), v is the scan rate, i denotes the current measured at each scanning rate,

while k_1 and k_2 are constants. The k_1v and $k_2v^{0.5}$ respectively stand for the contributions of the surface capacitance process and the diffusion insertion process [25]. The b-values for both PB and PB@C are close to 1, suggesting that the kinetics of the surface capacitive process are rapid and play a more significant role. As shown in Figure 2c and d, for peak a, the proportion of capacitance contribution varies across different scan rates, exhibiting a steady increase as the scan rate escalates. Specifically, the PB@C cathode exhibits a capacitance contribution of 51% at a scan rate of 0.1 mV s^{-1}, increasing to 80.55% at a scan rate of 1.0 mV s^{-1}. Conversely, the PB cathode displays a capacitance contribution of 40.3% at a scan rate of 0.1 mV s^{-1} and rises to 70.19% at a scan rate of 1.0 mV s^{-1}. The prominence of capacitive contributions becomes increasingly evident at elevated scan rates. These observations imply that the PB@C cathode displays exceptional pseudocapacitive behavior and facilitates swift Na^+ diffusion amidst the charging and discharging procedures, aligning with its high-rate performance capabilities. At a scan rate of 0.1 mV s^{-1}, the contributions of surface capacitive process of PB and PB@C are shown in Figure 2e and 2f. Once coated with carbon sol, the surface capacitive contribution of PB at a scanning rate of 0.1 mV s^{-1} escalated from 40.3% to 52.1%. Both b-value and surface capacitance suggest that the PB@C cathode exhibits swifter kinetic properties. This rapid kinetic enhancement is attributed to the inclusion of carbon, leading to superior rate performance.

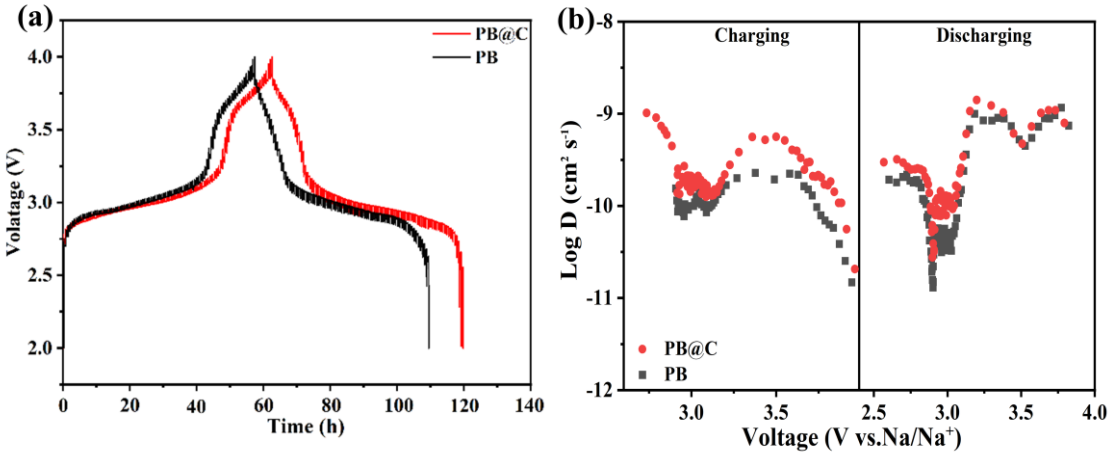

Figure 3: (a) GITT and (b) DNa+ curves of PB@C and PB.

To understand the diffusion rate of sodium ions in the PB@C and PB cathodes, the D_{Na+} during the intercalation/de-intercalation process was verified using GITT. The D_{Na+} can be calculated according to Fick's second law [26]. As shown in Figure 3a and 3b, the D_{Na+} for the PB@C cathode during the charge-discharge process is calculated to be approximately in the range of 10-9 to 10^{-10} cm^2 s^{-1}. For the PB cathode, the D_{Na+} primarily concentrates around 10^{-10} cm $^2s^{-1}$. Clearly, the D_{Na+} for the PB@C cathode is significantly higher than that of the PB cathode, indicating that the PB@C cathode exhibits faster diffusion kinetics during charge and discharge cycles, which enhances its superior electrochemical performance.

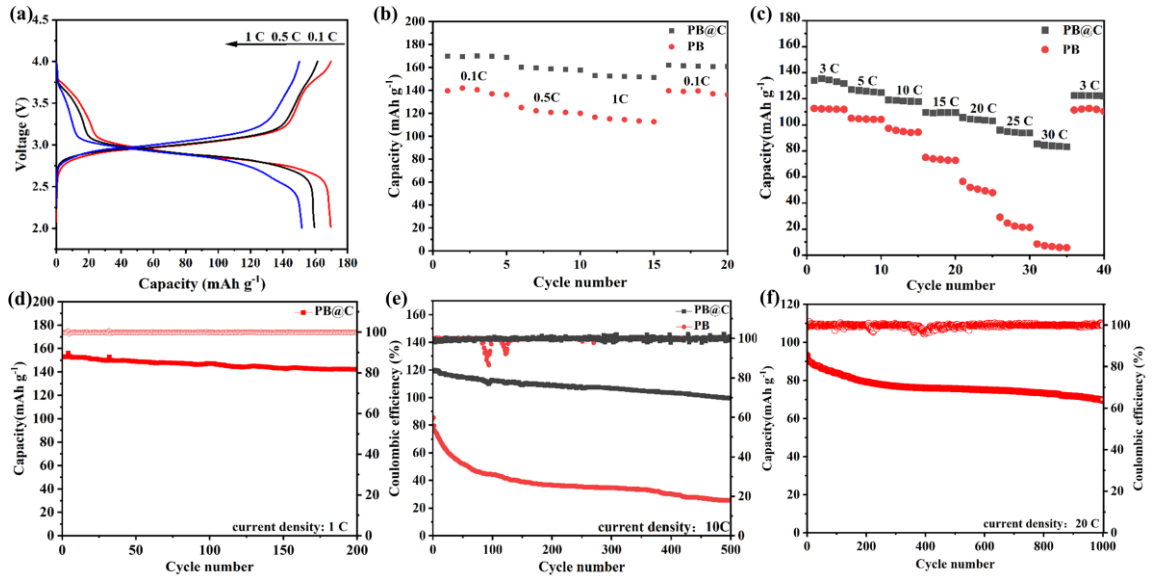

Figure 4: (a) The charge-discharge curves of PB@C from 0.1C to 1C; (b) PB@C and PB at low rate performance; (c) Performance comparison of PB@C and PB under different rates; (d) Cyclic performance of PB@C at 1C; (e) Long-cycle comparison of PB@C and PB at a current density of 10C; (f) The long-cycle performance of PB@C at a high rate of 20C.

Figure 4a show the charge-discharge voltage profile of PB@C. The long charge-discharge plateau within the scope of 2.6 - 3.1 V is attributed to the redox reaction of Fe^{2+}/Fe^{3+}, corresponding to the oxidation-reduction peak on the CV curve. In Figure 4b, the PB@C cathode was charged and discharged at current densities ranging from 0.1C to 1C, and its discharge specific capacities were 169, 159, and 151 mAh g^{-1}, respectively. In comparison, the discharge specific capacities of the PB cathode at the same rates are 140, 124, and 117 mAh g^{-1}, respectively. Evidently, after carbon sol was coated on PB, the initial discharge capacity undergoes a notable enhancement, escalating from 140 to 169 mAh g^{-1} at a rate of 0.1C. This augmentation closely approximates the theoretical capacity of 170 mAh g^{-1}.

Figure 4c illustrates the rate performance comparison between the PB and PB@C cathodes across various discharge rates. The capacities of the PB cathode at 3C, 5C, 10C, 15C, 20C, 25C, and 30C are 112.5, 104.9, 97.2, 73.5, 56.4, 29.8, and 8.7 mAh g^{-1}, respectively. The PB cathode is capable of sustaining a substantial capacity when operated at low rates; however, its electrochemical performance undergoes a precipitous decline when subjected to high rates, and it virtually loses all capacity beyond 20C. In contrast, the capacities of the PB@C cathode at 3C, 5C, 10C, 15C, 20C, 25C, and 30C are 134.5, 127, 119.03, 109.4, 105.5, 94.8, and 85.3 mAh g^{-1}, respectively. Obviously, the PB@C cathode demonstrates a higher capacity than the PB cathode at various rates, particularly at high rates. When the rate reverts to 3C, the discharge capacity of the PB@C cathode is restored to an impressive 122.55 mAh g^{-1}, marginally lower than its original discharge capacity at 3C, highlighting the exceptional electrochemical reversibility of the PB@C cathode. Remarkably, it has been observed that the PB@C cathode continues to exhibit impressive discharge capacities of 94.8 and 85.3 mAh g^{-1} at 25 and 30C rates, respectively. In contrast, the discharge capacities of the PB cathode are significantly lower, at merely 29.8 and 8.7 mAh g^{-1}, under the same current rates. The outstanding rate performance suggests its good structural stability. The PB@C cathode exhibits a remarkable specific capacity and superior cycling performance at low rates. Following 200 cycles at a 1C, it sustains an impressive capacity retention rate of 92% (Figure 4d). Regarding the PB@C cathode, its exceptional electrochemical reversibility is

fundamentally attributed to the inherent robust electronic conductivity of the carbon-based material, which facilitates the swift diffusion of Na^+ ions between the electrolyte and the extensive lattice structure, ensuring minimal energy losses.

Figure 4e presents a comparison of the long-cycle performance between the PB@C and PB cathodes at 10C. The capacity of the PB cathode decays rapidly in the first 100 cycles, while the PB@C cathode maintains a stable capacity, and the capacity retention after 500 cycles is 83%, with discharge-specific capacity of 99.5mAh g^{-1}, which significantly exceeds that of the PB cathode. The findings indicate that the crystal structure of PB@C remains intact and exhibits exceptional long-term cycling stability, due to the presence of the protective carbon coating layer. Figure 4f further delineates the long-term cycling performance of PB@C at a high rate of 20C. Following 1000 cycles, the capacity retention rate amounts to 76.7%, accompanied by a discharge specific capacity of 70 mAh g^{-1}. The results suggest that the incorporation of carbon coating layer enhances the surface capacitive contribution, thereby boosting kinetic performance and effectively mitigating capacity degradation.

4. Conclusion

In conclusion, a straightforward synthesis technique was utilized to produce a carbon sol, which was subsequently applied to coat the surface of PB, resulting in the successful fabrication of PB@C cathode material. The introduction of the carbon coating layer boosts the electronic conductivity and suppresses the side reactions between the electrolyte and the electrode material. The results show that the obtained PB@C cathode exhibited superior sodium storage performance. The specific capacity of PB@C reaches 85 mAh g^{-1} at a discharge rate of 30C. Moreover, it maintains 83% of its capacity after 500 cycles at 10 C and 76.7% after 1000 cycles at 20C, representing a significant enhancement over the unmodified PB cathode. The findings imply that the application of a carbon sol coating substantially boosts the electrochemical performance of PB, indicating a viable approach for modifying PB at low temperature.

Acknowledgements

This work is financially supported by the National Natural Science Foundation of China (22362006), the Natural Science Foundation of Guangxi Province (2023GXNSFAA026444), and the Guangxi Minzu University Research Funding Project (2022KJQD36, 2022MDKJ005).

References

[1] J.B. Goodenough, How we made the Li-ion rechargeable battery, Nat. Electron. 1 (2018) 204.
[2] M. Li, J. Lu, Z. Chen, K. Amine, 30 Years of Lithium-Ion Batteries, Adv. Mater. 30 (2018) 1800561.
[3] N. Yabuuchi, K. Kubota, M. Dahbi, S. Komaba, Research Development on Sodium-Ion Batteries, Chem. Rev. 114(2014) 11636–11682.
[4] P.K. Nayak, L. Yang, W. Brehm, P. Adelhelm, From Lithium-Ion to Sodium-Ion Batteries: Advantages, Challenges, and Surprises, Angew. Chem. Int. Ed. 57 (2018) 102–120.
[5] B. Dunn, H. Kamath, J.-M. Tarascon, Electrical Energy Storage for the Grid: A Battery of Choices, Science 334 (2011) 928–935.
[6] X.N. Xie, Y. Wang, Q. Wang, K.P. Loh, A Percolating Membrane with Superior Polarization and Power Retention for Rechargeable Energy Storage, Adv. Mater. 24 (2012) 76–81.
[7] C. Zhao, Q. Wang, Z. Yao, J. Wang, B. Sánchez-Lengeling, F. Ding, X. Qi, Y. Lu, X. Bai, B. Li, H. Li, A. Aspuru-Guzik, X. Huang, C. Delmas, M. Wagemaker, L. Chen, Y.-S. Hu, Rational design of layered oxide materials for sodium-ion batteries, Science 370 (2020) 708–711.
[8] L. Mu, X. Feng, R. Kou, Y. Zhang, H. Guo, C. Tian, C. Sun, X. Du, D. Nordlund, H.L. Xin, F. Lin, Deciphering the Cathode–Electrolyte Interfacial Chemistry in Sodium Layered Cathode Materials, Adv. Energy Mater. 8 (2018) 1801975.

[9] L. Wang, J. Song, R. Qiao, L.A. Wray, M.A. Hossain, Y.-D. Chuang, W. Yang, Y. Lu, D. Evans, J.-J. Lee, S. Vail, X. Zhao, M. Nishijima, S. Kakimoto, J.B. Goodenough, Rhombohedral Prussian White as Cathode for Rechargeable Sodium-Ion Batteries, J. Am. Chem. Soc. 137 (2015) 2548–2554.
[10] X. Wu, W. Deng, J. Qian, Y. Cao, X. Ai, H. Yang, Single-crystal FeFe(CN)6 nanoparticles: a high capacity and high rate cathode for Na-ion batteries, J. Mater. Chem. A 1 (2013) 10130.
[11] F. Bu, X. Feng, T.Jiang, I. Shakir, Y. Xu ,One Versatile Route to Three-Dimensional Graphene Wrapped Metal Cyanide Aerogels for Enhanced Sodium Ion Storage, Chem. Eur. J. 23(2017) 8358-8363.
[12] Y. Jiang, S. Yu, B. Wang, Y. Li, W. Sun, Y. Lu, M. Yan, B. Song, S. Dou, Prussian Blue@C Composite as an Ultrahigh-Rate and Long-Life Sodium-Ion Battery Cathode, Adv. Funct. Mater. 26 (2016) 5315–5321.
[13] Y. You, H. Yao, S. Xin, Y. Yin, T. Zuo, C. Yang, Y. Guo, Y. Cui, L. Wan, J.B. Goodenough, Subzero-Temperature Cathode for a Sodium-Ion Battery, Adv. Mater. 28 (2016) 7243–7248.
[14] J. Luo, S. Sun, J. Peng, B. Liu, Y. Huang, K. Wang, Q. Zhang, Y. Li, Y. Jin, Y. Liu, Y. Qiu, Q. Li, J. Han, Y. Huang, Graphene-Roll-Wrapped Prussian Blue Nanospheres as a High-Performance Binder-Free Cathode for Sodium-Ion Batteries, ACS Appl. Mater. Interfaces 9 (2017) 25317–25322.
[15] W. Duan, Z. Zhu, H. Li, Z. Hu, K. Zhang, F. Cheng, J. Chen, Na3V2(PO4)3@C core–shell nanocomposites for rechargeable sodium-ion batteries, J. Mater. Chem. A 2 (2014) 8668-8675.
[16] L. Nayak, M. Rahaman, R. Giri, Surface Modification/Functionalization of Carbon Materials by Different Techniques: An Overview. Carbon-Containing Polymer Composites; Springer, 2019; pp 65−98.
[17] L. Deng, G. Sun, K. Goh, L.-L. Zheng, F.-D. Yu, X.-L. Sui, L. Zhao, Z.-B. Wang, Facile one-step carbothermal reduction synthesis of Na3V2(PO4)2F3/C serving as cathode for sodium ion batteries, Electrochim. Acta 298 (2019) 459–467.
[18] Q. Liu, X. Meng, Z. Wei, D. Wang, Y. Gao, Y. Wei, F. Du, G. Chen, Core/Double-Shell Structured Na3V2(PO4)2F3@C Nanocomposite as the High Power and Long Lifespan Cathode for Sodium-Ion Batteries, ACS Appl. Mater. Interfaces 8 (2016) 31709–31715.
[19] Y. You, X.-L. Wu, Y.-X. Yin, Y.-G. Guo, High-quality Prussian blue crystals as superior cathode materials for room-temperature sodium-ion batteries, Energy Environ. Sci. 7 (2014) 1643–1647.
[20] R. Behling, S. Valange, G. Chatel, Heterogeneous catalytic oxidation for lignin valorization into valuable chemicals: what results? What limitations? What trends? Green Chem. 18 (2016) 1839–1854.
[21] Y. Jiang, S. Yu, B. Wang, Y. Li, W. Sun, Y. Lu, M. Yan, B. Song, S. Dou, Prussian Blue@C Composite as an Ultrahigh-Rate and Long-Life Sodium-Ion Battery Cathode, Adv. Funct. Mater. 26 (2016) 5315–5321.
[22] D. Su, K. Kretschmer, G. Wang, Improved Electrochemical Performance of Na-Ion Batteries in Ether-Based Electrolytes: A Case Study of ZnS Nanospheres, Adv. Energy Mater. 6 (2016) 1501785.
[23] H.B. Wu, J.S. Chen, H.H. Hng, X.W. Lou, Nanostructured metal oxide-based materials as advanced anodes for lithium-ion batteries, Nanoscale 4 (2012) 2526.
[24] J. Wang, J. Polleux, J. Lim, B. Dunn, Pseudocapacitive Contributions to Electrochemical Energy Storage in TiO2 (Anatase) Nanoparticles, J. Phys. Chem. C 111 (2007) 14925–14931.
[25] A. Vasileff, S. Chen, S.Z. Qiao, Three dimensional nitrogen-doped graphene hydrogels with in situ deposited cobalt phosphate nanoclusters for efficient oxygen evolution in a neutral electrolyte, Nanoscale Horiz. 1 (2016) 41–44.
[26] L.-L. Zhang, Z.-Y. Chen, X.-Y. Fu, B. Yan, H.-C. Tao, X.-L. Yang, Effect of Zn-substitution induced structural regulation on sodium storage performance of Fe-based Prussian blue, Chem. Eng. J. 433 (2022) 133739.